Title: Role of inhibitory control in modulating spread of focal ictal activity

Authors: Jyun-you Liou[1], Hongtao Ma[2], Michael Wenzel[3], Mingrui Zhao[2], Eliza Baird-Daniel[2],

Elliot H Smith[4], Andy Daniel[2], Ronald Emerson[5], Rafael Yuste[3], Theodore H Schwartz[2,*] ,

Catherine A Schevon[6,*]

*These authors contributed equally to the work.

Corresponding author: Catherine Schevon

Address:

710 West 168th Street

New York, NY 10032

(212) 305-2121

Email: cas2044@cumc.columbia.edu

Affiliations:

1. Department of Physiology and Cellular Biophysics, Columbia University, New York, NY

    10032, USA

2. Department of Neurological Surgery, Feil Family Brain and Mind Research Institute,

    Sackler Brain and Spine Institute, Weill Cornell Medicine, New York-Presbyterian

    Hospital, , New York, NY 10065, USA

3. Neurotechnology Center, Department of Biological Sciences, Columbia University, New

    York, NY 10027, USA; Department of Neuroscience, Columbia University, New York, NY

    10032, USA.

4. Department of Neurological Surgery, Columbia University Medical Center, New York, NY, 10032, USA.

5. Hospital for Special Surgery, 535 East 70th Street, New York, NY 10021, USA.

6. Department of Neurology, Columbia University Medical Center, New York, New York 10032, USA.

Abstract

Focal seizure propagation is classically thought to be spatially contiguous. However, propagation through the epileptic network – a collection of disparate epileptic nodes – has been theorized. Here, we used a multielectrode array, wide field calcium imaging, and two-photon calcium imaging to study focal seizure propagation pathways in an acute rodent neocortical 4-aminopyridine model. Although ictal neuronal bursts were limited to a 2-3 mm region without clear propagation, they were associated with hemisphere-wide LFP fluctuations and parvalbumin-positive interneuron activity outside the seizure focus. Globally compromising this inhibitory response using bicuculline surface application resulted in classical contiguous propagation; whereas, focal bicuculline microinjection resulted in epileptic network formation with two physically disparate foci. Our study suggests both classical and epileptic network propagation could arise from inhibition defects without pre-existing pathological connectivity changes, and that preferred propagation pathways may result from variations in cortical topology.

Introduction

The topology of seizure propagation has long been debated, and may depend on factors such as cortical connectivity and underlying pathology. Classically, seizures are thought to spread to physically contiguous regions, expanding in a sequential manner through progressive recruitment of adjacent cortical circuitry (Figure 1A). This progression manifests clinically during the well-known Jacksonian march (Extercatte et al., 2015), has been extensively documented in animal models, both in vivo and in vitro (Bikson et al., 2003; Pinto et al., 2005; Trevelyan et al., 2006; Trevelyan et al., 2007b), and was recently demonstrated in spontaneous human seizures (Schevon et al., 2012; Smith et al., 2016). In contrast to this classical view, propagation through 'epileptic networks' – presumed pathological connections of dispersed cortical regions (Figure 1B) – has also been recently proposed and supported by both imaging and intracranial low-frequency EEG studies (Khambhati et al., 2016; Kramer et al., 2010; Luo et al., 2014). These observations raise unanswered questions such as how neural activity in disparate cortical regions synchronizes, whether pathological connectivity is required, and precisely how epileptic activity propagates through long-range cortico-cortical connections.

Epileptiform discharges during focal seizures can be observed at a significantly larger spatial scale than its neuronal substrates. This has been traditionally ascribed to a passive volume conduction process. However, analyses of in vivo human microelectrode recordings demonstrate that the widespread synaptic barrages emanating from a small ictal core may more accurately explain the spatial discrepancy (Schevon et al., 2012; Weiss et al., 2013). Detailed in vitro brain slice studies have shown that in normal tissue, a fast, strong inhibitory conductance prevents the distributed synaptic activity from triggering ictal activity (Trevelyan

et al., 2006; Trevelyan et al., 2007b), and evidence of the same process has been detected in humans (Schevon et al., 2012). The in vivo 4-aminopyridine (4-AP) seizure model has also suggested widespread projections from a localized ictal event, as shown by its large-scale propagating waves and neurovascular coupling effects (Bahar et al., 2006; Ma et al., 2013; Ma et al., 2009; Zhao et al., 2009; Zhao et al., 2011). Given the electrographic similarity of 4-AP ictal events to human neocortical-onset seizures, the area of bursting cells, i.e. the 4-AP ictal core, should also be significantly smaller than the region demonstrating epileptiform discharges. However, relevant evidence is still lacking.

Here, we assess the effects of ictal activity projection at varying cortical distances, as well as inhibitory responses using multielectrode arrays, wide field calcium imaging, and two-photon calcium imaging of interneurons in the acute rodent in vivo 4-AP model, using bicuculline methiodide (BMI) to block GABA-A activity at varying distances from the core. We hypothesize that strongly excitatory synaptic projections arise from the ictal core and are distributed widely, but are normally masked by local inhibitory responses. We propose that seizure propagation can proceed via two topologically distinct patterns that both depend on the inhibition breakdown process: one involving slow (< 1 mm/sec), contiguous spread and the other operating across large distances at much greater speeds. Sites in which inhibitory responses are compromised determine whether seizures can propagate and their topological sequence. This provides a plausible mechanism reconciling the longstanding, classical contiguous seizure propagation patterns with the observed large-scale epileptic network behavior during human seizures (Smith and Schevon, 2016).

Figure 1. Two topological patterns of focal seizure propagation.
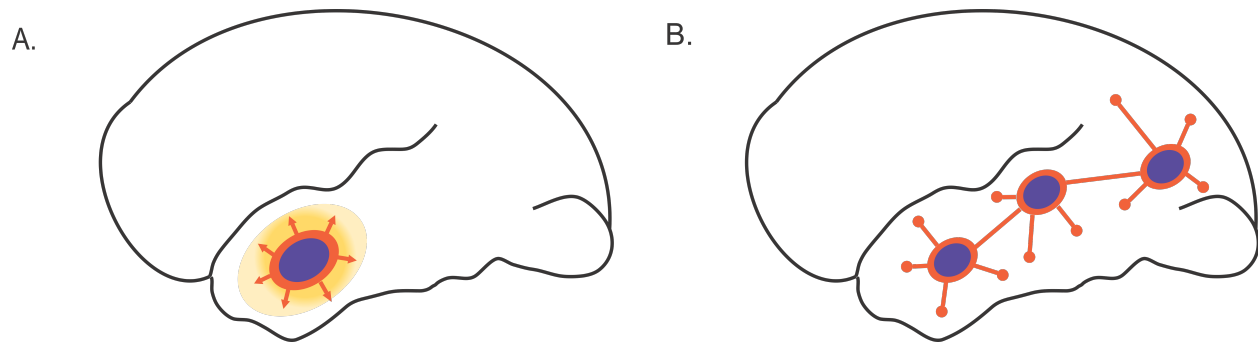
A. Classical, Jacksonian-like focal seizure propagation. The purple zone is the ictal core, surrounded by the ictal wavefront (orange), slowly expanding toward adjacent cortical circuitry. The yellowish area surrounding the ictal core represents the 'ictal penumbra', an area that receives massive synaptic barrages from the ictal core but has not been recruited into the seizing territory.

B. The epileptic network. Several disparate ictogenic zones (purple) are recurrently connected by synaptic projections (orange lines). Focal seizure activity may arise from coordinated activity and propagate to disparate regions through distributed mechanisms.

Results

Focal 4-AP injection induced spatially constrained ictal events

Figure 2A shows the experimental setup. Injecting 15mM, 500 nL 4-AP into somatosensory cortex of adult Sprague-Dawley rats induced focal ictal activity (Figure 2B-2C). LFPs with maximal line length (the ictal center) were detected at the area where 4AP was injected (Figure 2B, anterior-right corner of the array). At the same region, multiunit unit firing rate increased (Figure 2C). During ictal events, similar to human focal seizures (Merricks et al., 2015), the waveforms of multiunit spikes near the ictal center were distorted (light blue arrows in Figure 2C); whereas waveforms of multiunit spikes detected distally were preserved (yellow arrows in Figure 2C), indicating regional differences. The spatial extension of the LFP activities remained stable during repetitive ictal events (Figure 2D). Overall, both LFP activity and multiunit firing rates decreased sharply with increasing distance from the 4-AP injection site in all experiments (Figure 2E & 2F), indicating that the 4-AP model is well-defined and limited to a small area adjacent to the injection site. Beyond the spatial extent of the seizure focus, LFP recordings still showed minor increase of line length (Figure 2E, posterior rows of electrodes), yet the average multiunit firing was not significantly greater than baseline (Figure 2F, see legends for detailed statistics).

Figure 2. Multielectrode array recordings demonstrating focal nature of 4-AP ictal events
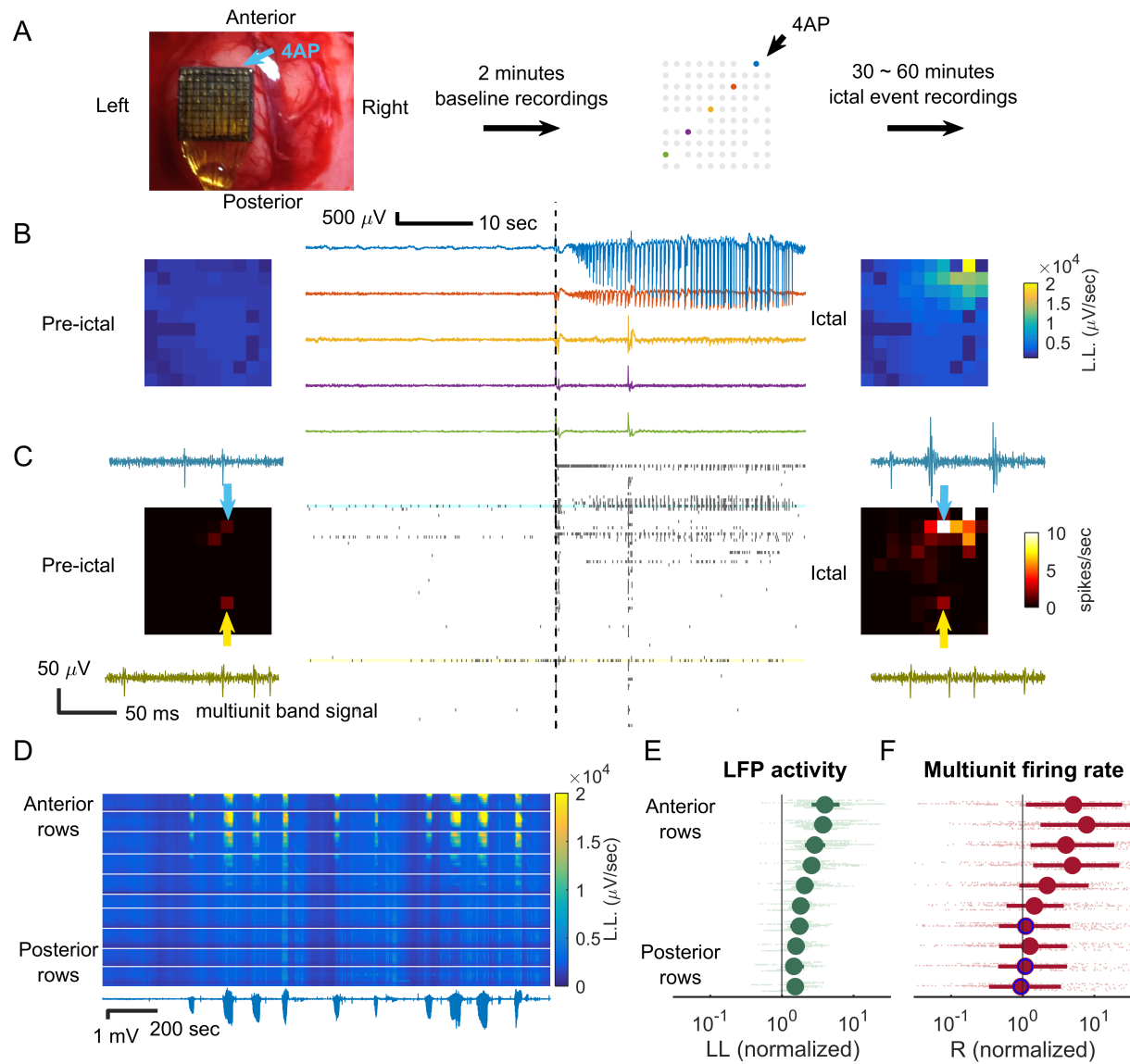
A. Experimental setup. The multielectrode array (96 electrodes, arranged in a 10 by 10 grid, with orthogonal interelectrode spacing of 400 microns) was implanted in the left hemisphere. A two-minute baseline recording was obtained. 4-AP was the injected at the anterior border (upper right corner) to induce ictal events. Missing dots denote

non-recording electrode sites. Five microelectrodes are highlighted with a color code corresponding to traces shown in ensuing panels.

B. Sample LFP recordings of pre-ictal (left) and ictal (right) periods after 4AP injection. The line length (LL) measure is used in corresponding color spectrum plots to show the spatial layout of ictal activity. Again, note the focality of the event.

C. Raster plot of multiunit firing during pre-ictal (left) and ictal (right) periods. The time axis (horizontal) aligns with Panel B. Average multiunit firing rates are shown in the corresponding heat maps. The multiunit band signal of sample channels (light blue and yellow) are showed in the subpanels. Note the focality of the event.

D. Repetitive ictal events from one animal are shown. Ictal activities were similarly spatially distributed - concentrated at the anterior region sampled by the multielectrode array. Lower trace: LFP recording from the ictal center (highest line length). In the corresponding color map, each row represents one channel, arranged according to distance from the anterior edge of the microelectrode array. Activity is denoted by line-length averaged over 5 second moving windows.

E. Quantification of ictal activities along the anterior-posterior axis (8 animals, 150 ictal events, marker: median, error bar: interquartile range). For each ictal event, the average line-length of each channel, divided by its baseline line length, is plotted along the horizontal axis and the electrode's physical position, anterior-posteriorly, is plotted along the vertical axis. Each animal's data are plotted with minor vertical offsets to facilitate visualization. Green markers and error bars represent the electrode row-specific median and interquartile ranges of the 150 ictal events. During ictal events, LFP

activities showed general increase (for each row, sign test under null hypothesis $LL_{ictal\ events} = LL_{baseline}$: p<0.001) with clear anterior-posterior gradient (Spearman's correlation coefficient between a channel's anterior-posterior position and its line-length during ictal events: 0.59, 8 animals, N=8909, p << 0.001).

F. Quantification of multiunit firing rate along the anterior-posterior axis (8 animals, 150 ictal events). Panel presentation conventions were adopted from Panel E. The anterior channels showed significant multiunit firing rate increase (sign test under null hypothesis $R_{ictal\ events} = R_{baseline}$: p<0.001) but not the posterior channels (markers with blue rims, p = 0.26, 0.07, and 0.53 from anterior to posterior respectively). Spearman's correlation coefficient again confirmed the existence of anterior-posterior gradient of (ρ=0.31, 8 animals, N=3915, p << 0.001).

Wide-field calcium imaging confirmed 4AP ictal event's focal nature is regionally invariant

Multielectrode array studies are limited in spatial sampling (4 by 4 mm) and resolution (400 microns). To overcome these limitations, we used wide-field calcium imaging to obtain a comprehensive, high-resolution spatial map of neural activity during ictal events (Figure 3A-C). Wide-field calcium imaging revealed a similar focal onset and limited spread of calcium activity around the area of the 4-AP injection (Figure 3B). A sharp demarcation of neural activity occurred roughly 2-3 mm from the injection site, providing a real-time map of the evolving ictal focus (Figure 3D). Notice here we injected 4-AP in visual cortex instead of somatosensory cortex, which confirmed 4-AP ictal event's focal nature is regionally invariant.

Figure 3. Wide field calcium imaging confirmed focal nature of 4AP ictal events.
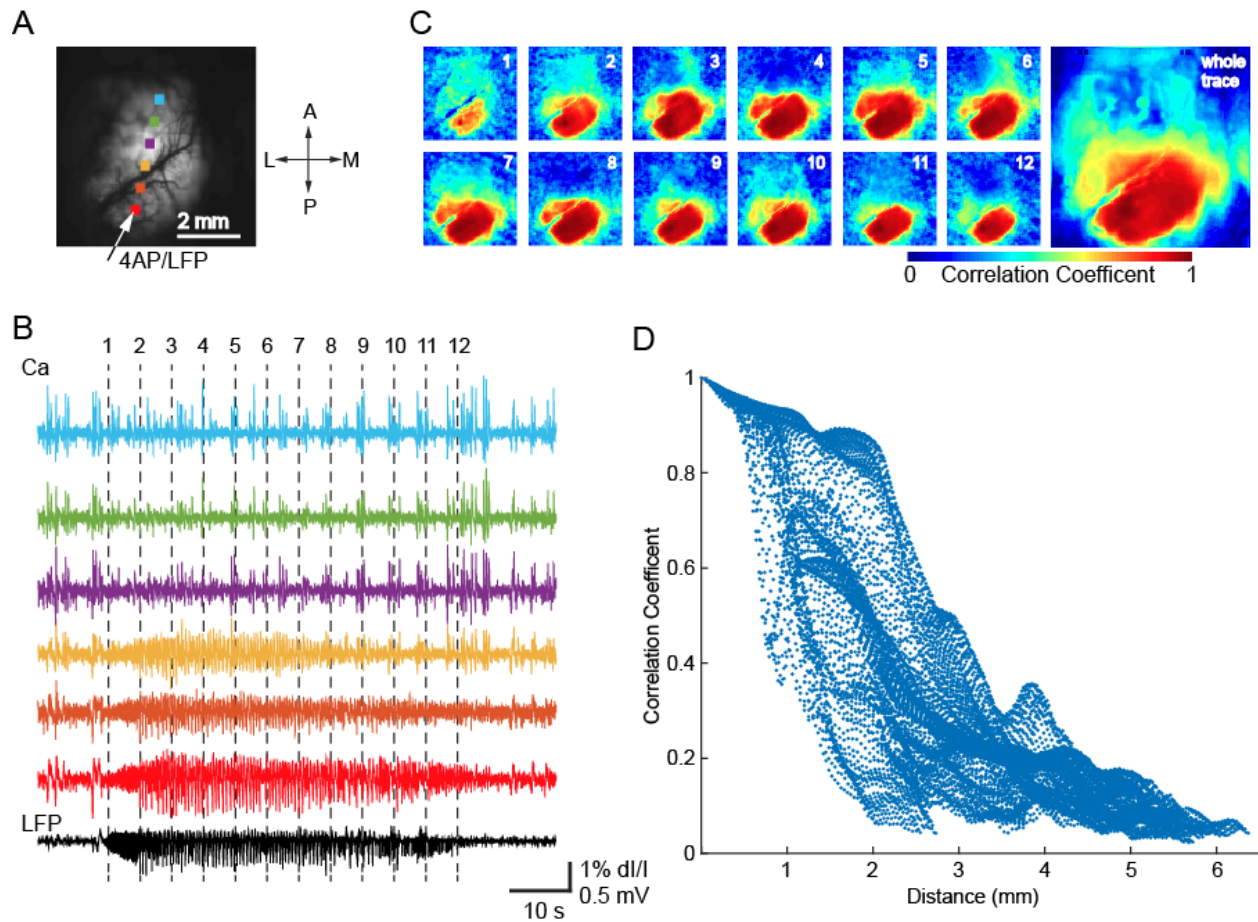
A. The field of view. The arrow at the bottom left corner shows the location of 4AP/LFP electrode. Six color dots show the locations of the regions of interest (ROIs) where the calcium traces are shown in Panel B.

B. The LFP (black, bottom trace) and calcium fluorescence (colored traces above, 1 Hz high pass) during an ictal event. 12 vertical dotted line showed 12 different time points during the ictal event evolution, which are used to generate the maps in Panel C. Notice the bottom 3 traces (proximal) show a similar waveform as the LFP recording; whereas

the top 3 traces (distal) showed intermittent bursting neural activity that were dissociated from the LFP.

C. The spatiotemporal evolution of the calcium activity during an ictal event. Left: The color maps showed the seed-initiated correlation coefficient maps during 12 different time points. Note the focal onset and limited spread of the calcium signal with high correlation coefficient around the 4-AP electrode, supporting the focal nature of 4-AP ictal events. Right: The color map of seed initiated correlation coefficient map of the whole trace.

D. Graph of the Pearson correlation coefficient between each pixel's calcium fluorescence and the LFP tracing based on the distance of each pixel from the location of the LFP electrode. Note a sharp decrease of calcium signal that occurs around 2-3 mm from the 4AP injection.

Multiunit activity at the ictal focus is associated with hemisphere-wide, distance-dependent LFP responses

The focal nature of 4-AP ictal events provided the opportunity to investigate neural responses at various distances from the focus. During 4-AP ictal events, multiunit firing near the ictal center ($\leq$1 mm) was associated with LFP fluctuations both locally and distally (Figure 4A). Spike-triggered averaging (Figure 4B) demonstrated distance dependence with respect to polarity and temporal delay. Electrodes proximal to the ictal center ($\leq 1mm$) showed large negative LFP deflections which peaked shortly after multiunit firing bursts (Figure 4B, blue

traces; median peak times: 4.3 ms, interquartile range: 3.5 to 5.4 ms; Figure 4C, blue arrows).

Distally (> 4mm), there were positive deflections with prolonged delays (Figure 4B, green traces; median peak times: 17.6 ms, interquartile range: 14.9 to 18.9 ms; Figure 4C, red arrows). The distance-dependent polarity switch (Figure 4D, left subpanel, blue to red arrows) and temporal delay (Figure 4D, right subpanel, blue to red arrows) were observed across experiments (8 animals, 150 ictal events).

Figure 4. Multiunit activities inside the ictal focus were associated with hemisphere-scale, distance-dependent LFP responses.
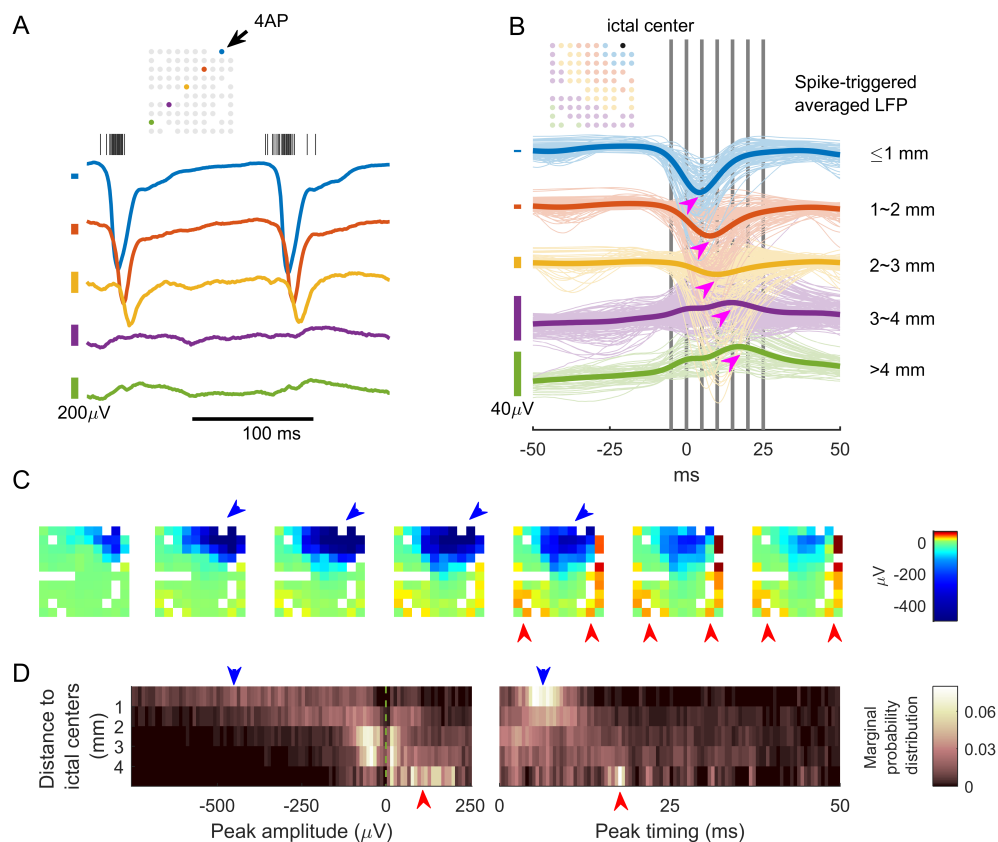
A. Sample LFP traces with ictal multiunit activity. Traces are scaled according to the vertical scale bars at the left side. The centers of the scale bar are the isoelectric points

for traces that have the same color. The LFP trace colors indicate where they were recorded from, as shown in the array schematic.

B. Spike-triggered LFP in one animal, averaged over 11 ictal events. Colors are used to mark LFP traces' distance from the ictal center. The thick lines are the average of traces with similar colors. Notice the sequential increase of temporal delay of peak response and the switch of polarity (magenta arrows) as distance increases. Blue traces median temporal delay, measured as the timing of the negative peaks: 4.3 ms (3.5 to 5.4 ms, n = 88). Green traces median temporal delay, measured as the timing of the positive peaks: 17.6 ms (14.9 to 18.9 ms, n = 55). U-test comparing the median between the two groups showed p << 0.001. Vertical gray bars are used to indicate the timing of the frames in Panel C.

C. The spatiotemporal evolution of spike-triggered averaged LFP. Each frame's time is indicated by Panel B's vertical gray bars from left to right sequentially. Large negative LFP deflections were found near the ictal center (blue arrows) whereas positive LFP deflections were found distal to the ictal center, and with increased/different temporal delay (red arrows).

D. Summary of spike-triggered averaging studies in 8 animals, 150 ictal events. For each channel during each ictal event, the spike-triggered LFP's global extremum (where the signal deviated from isoelectric point the most) was recorded. The search range for global extrema was limited within the causal part of the signal (0 to +50 ms). Data were grouped by distance and their extrema's distribution were shown in the heat maps (N = 1131, 1506, 2263, 1515, and 346 from proximal to distal groups). Left subpanel:

distribution of extrema value, notice the switch of polarity (Probability of detecting a negative peak = 0.93*, 0.75*, 0.58*, 0.45, 0.14*, sign test, α=0.05). Right subpanel: distribution of peak timing, notice the temporal delay (median: 6.9, 8.7, 10, 14.9, 17.5 ms, Kruskal–Wallis test p < 0.001).

Parvalbumin(+) interneurons may contribute to surround inhibition effect of ictal events

We therefore confirmed that focal ictal events exert widespread, hemisphere-scale effects, reflected in the associated LFP fluctuations. The observations of widespread, hemisphere-scale LFP effects and the proximal-distal polarity flip led us to hypothesize that ictal activities exert qualitatively opposite effects in distal compared to proximal neural tissues, and that the distal effect is inhibition-dominant (Marshall et al., 2016).   The greater distal temporal delay suggests that a multi-synaptic pathway is involved, consistent with feedforward inhibition. To test this hypothesis, we employed in vivo 2-photon calcium imaging to record the activity of parvalbumin (PV) positive interneurons in the distal surrounding tissue during ictal events (Figure 5). We selected PV(+) interneurons because of their strong inhibitory effect on pyramidal neurons through proximal dendrite and soma projections(Kepecs and Fishell, 2014; Markram et al., 2004). Also, PV(+) interneurons have been reported to restrain ictal propagation in acute brain slices (Cammarota et al., 2013; Sessolo et al., 2015). Upon 4-AP injection at visual cortices (to test regional invariance), the ictal events reliably activated PV(+) interneurons in distal region (4mm away from injection site, Figure 5B-D). The recruitment of distal PV(+) interneurons to electrographic ictal events occurred with little temporal delay

(Figure 5E-F, see legends for detailed statistics). The rapid response indicated that PV(+) interneurons are activated through synaptic transmission instead of slow processes such as extracellular ion diffusion. Overall, the observation of rapid PV(+) interneuron activation supported our hypothesis that ictal events exert net inhibitory effects on surrounding tissues.

Figure 5 **In vivo two-photon sub-population calcium imaging shows rapid recruitment of distal PV(+) interneurons to ictal events.**
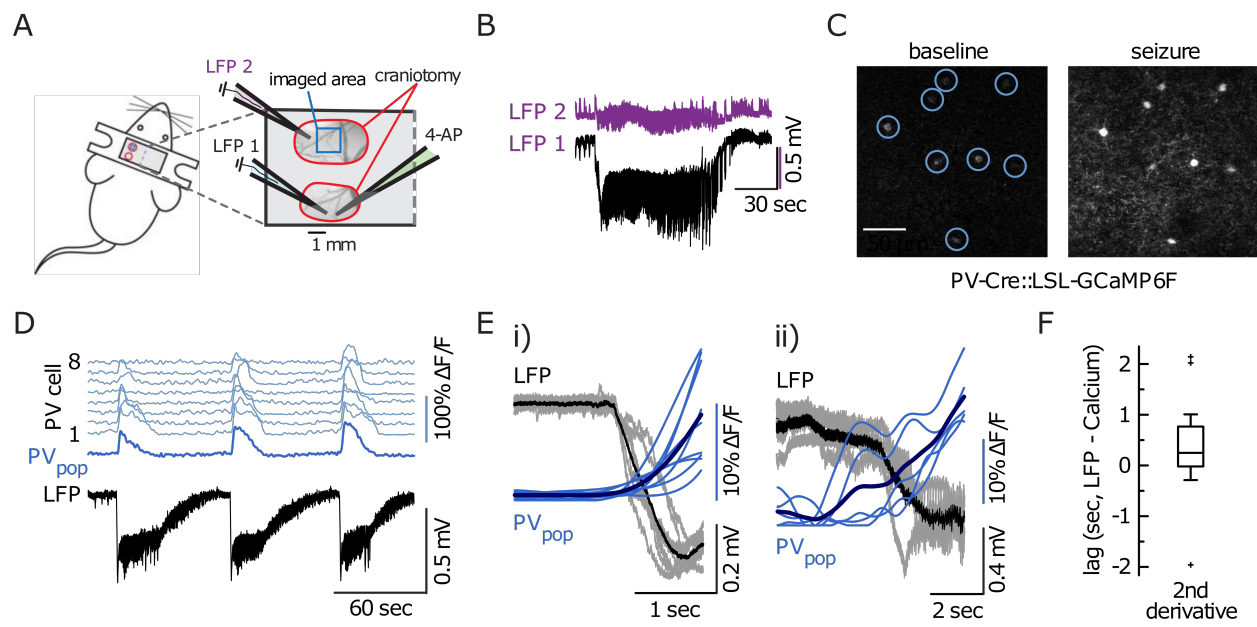
A. Experimental setup: Two craniotomies over left somatosensory and visual cortex, respectively; each craniotomy is encircled in red; imaging field of view (FOV) outlined in blue. In addition to PV(+) subpopulation imaging, experiments involved the insertion of either two or three glass micropipettes: one pipette containing 4-AP (green, 15mM, injection volume 500 nL), and one (injection site [LFP 1, light blue]) or two (injection site [LFP 1, light blue] plus imaging site [LFP 2, purple]) pipettes each containing a silver chloride silver for LFP recordings.

B. Two simultaneous LFP recordings (LFP 2 [purple] close by the imaging area, LFP 1 [black] proximal to 4-AP injection site). In line with experiments carried out in rats, there is a drastic reduction in amplitude and loss of DC-shift at the distal LFP electrode (inter-electrode distance ca. 4mm).

C. Representative 3 second average calcium images depicting 8 distal PVs during baseline (left) and during ictal onset (right). The increase in calcium is visible to the naked eye.

D. Calcium transients of the 8 PVs depicted in Panel C. Individual cells in light blue (top 8 traces), population average in dark blue. Simultaneous LFP recording near the 4AP injection site. Notice the consistent population recruitment across three consecutive ictal events.

E. Superposition of all electrographic ictal onsets and corresponding PV population calcium transients (blue, mean in dark blue) in two independent experiments (i=9 ictal events, ii=5 ictal events). Note the systematic relationship between the paroxysmal DC-shift in the LFP (ictal onset) and a clear rise in the PV population calcium signal.

F. Quantification of temporal PV population recruitment lag (distance to ictal initiation site ca. 4mm). PV onset time points were defined by maximum 2nd derivative of the calcium signal within the peri-ictal onset time window (which was determined electrographically). Box plot box depicts 25 – 75 %ile, horizontal bar within box represents the median (248.47 msec, interquartile range 786.44 msec; 2 animals, 14 ictal events). Outlier values are displayed as +.

Globally compromising GABA-A mediated fast inhibitory conductance causes massive contiguous ictal invasion

We subsequently tested the hypothesis that feedforward inhibition in the surrounding cortex is essential for preventing ictal propagation *in vivo*. We focused on pathways mediated by GABA-A conductance because of the short temporal delay shown in spike-triggered LFP studies is most consistent with GABA-A synaptic delay (Avoli and de Curtis, 2011; Lopantsev and Avoli, 1998; Pouille et al., 2013; Uva et al., 2005). To reduce GABA-A conductance, we first bathed the whole cranial window with 5mM bicuculline (BMI, a GABA-A receptor antagonist). As the BMI penetrated into the cortex, we observed that ictal events, originally well localized near the injection site (the first 3 events in Figure 6A-B, anterior-right corners), started to propagate outward contiguously (the later 3 events in Figure 6A-B, summarized in Figure 6C). By five minutes after BMI application (the right most episode), the ictal activity had invaded the entire area sampled by the microelectrode array. Notably, the morphology of the low-frequency LFP remained similar to the ictal events generated by 4-AP alone, as opposed to events triggered by focal BMI, which produces very high amplitude paroxysmal epileptiform discharges (Geneslaw et al., 2011; Ma et al., 2009; Ma et al., 2004) (also see later figures). Global BMI application also changed the multiunit activity pattern (Figure 6D). After BMI application, recording sites distant from the 4-AP injection site (lower rows of the raster plot), previously quiescent during ictal events, started to fire intensely during the ictal events but not between events. The recruitment followed spatial sequence and its speed increased over time (green versus magenta box in Figure 6D; Figure 6E, left panel). The sequential detection of multiunit spikes confirmed the ictal activity originated from the focus (Figure 6E, right panel)

and formed traveling waves spreading (Figure 6F) contiguously from the 4-AP injection site. In line with previous reports of ictal traveling waves in disinhibited rodent cortex (Chagnac-Amitai and Connors, 1989; Pinto et al., 2005; Trevelyan et al., 2007a), cross correlation of spike trains showed the average speed of the outward traveling waves was 63 mm/sec (Figure 6G-I, 95% confidence interval: 61.6 to 64.4 mm/sec).

Figure 6. Globally reducing inhibition strength causes contiguous ictal invasion
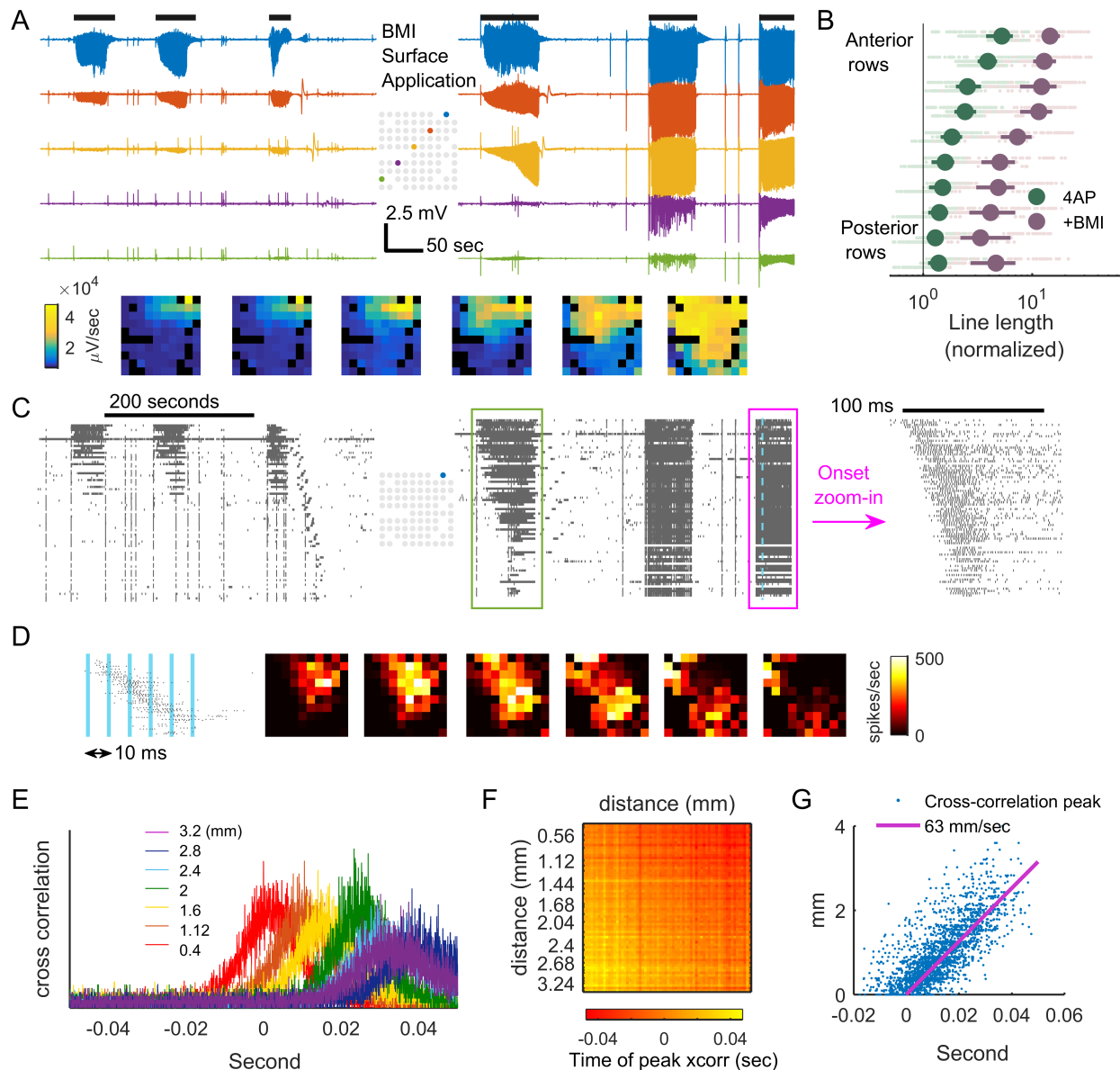
A. LFPs before (left) and after (right) BMI surface application. Horizontal black bars (upper part of the panel) indicate ictal periods. The spatial distributions of ictal activities during the 6 ictal events, measured in line-length, are shown in frames below sequentially.

B. Comparison of ictal activity (line length) before versus after BMI application. The panel's conventions are analogous to Figure 2E. Each light green and red dot represents data from one channel during one ictal event. Spearman correlation coefficient between a channel's position anterior-posteriorly and its line-length during ictal events after BMI application: 0.61. (3 animals, N = 1221, p << 0.001)

C. Multiunit activity before (left) and after (right) BMI surface application. Time is aligned with Panel A. Data are sorted so that the upper rows of the raster plot correspond to channels that are closer to the ictal center (blue electrode of the inlet map) and the lower rows correspond to distal channels. Green box: the first ictal event after BMI application. Notice the sequential recruitment of neurons from the 4-AP ictal center to distal areas. The ictal event marked with magenta box is zoomed in.   Notice the onset of the ictal event with spatially sequential recruitment from the 4-AP injection site, albeit at higher speed than the one in the green box.

D. The spatiotemporal evolution of a sample multiunit burst during an ictal event. The blue vertical bars indicate the timing of each frame. Notice the spread of the traveling wave pattern radiating from the 4-AP ictal center.

E. Cross-correlogram of the spike train recorded from the 4-AP ictal center to other channels during all ictal events (5 events) after BMI application. The colors indicate the distance between the channel's distance from the 4-AP ictal center.

F. The results of pairwise cross-correlation. For each channel pair, horizontal and vertical coordinates indicate each of the two channels' distance from the 4AP ictal center. Times of peak cross-correlation are indicated by color. Only channels that have shown a stable high average multiunit firing rate > 5 spike/sec are included here (66 channels).

G. Linear regression of data from Panel H. Linear regression model: $d_i - d_j = V * (t_i - t_j)$, where i & j are channel indices, d is the distance from the 4AP ictal center, and V is speed. Least squares regression shows V = 63 mm/sec, F-test p << 0.001, adjusted R^2 = 0.648 (66 channels, 2145 pairs).

The existence of long range excitatory pathways for ictal propagation

The observations of a distant (> 4mm) LFP signal (Figure 2B,2E, Figure 4) as well as triggered PV(+) interneuron activation activity (Figure 5) suggested a large-scale excitation pathway that extended further than the ictal zone's multiunit bursting and correlated calcium activity. We sought to investigate this further using a solitary, distant, focal BMI injection (5 mM, 500 nL). After establishing the 4-AP ictal focus, injecting BMI at the diagonal corner (the maximal distance our multielectrode array could record, i.e. $4\sqrt{2}$ mm) resulted in propagation of ictal activity toward the site of the BMI injection (Figures 7A). In this animal (21 ictal events), we were able to discern two physically separate but temporally linked foci (Figure 7A, magenta box), thus forming an artificially-induced epileptic network. Early during the sample ictal event (magenta box), the cortical territory between the two foci did not demonstrate multiunit bursting; indicating the ictal activity was not propagated contiguously (Figure 7B, early frames).

Instead, the in-between area was recruited antidromically (posterior to anterior, average speed: 0.19 mm/sec, 95% confidence interval: 0.17 to 0.21 mm/sec, 21 ictal events). The antidromic recruitment also indicated that the BMI foci constituted a second ictal core instead of simply mirroring projections from the 4-AP ictal focus.   The skipped, physically non-contiguous propagation pattern confirmed the existence of a long-range, epileptogenic excitatory pathway.

Figure 7. Ictal propagation pathway can be non-contiguous
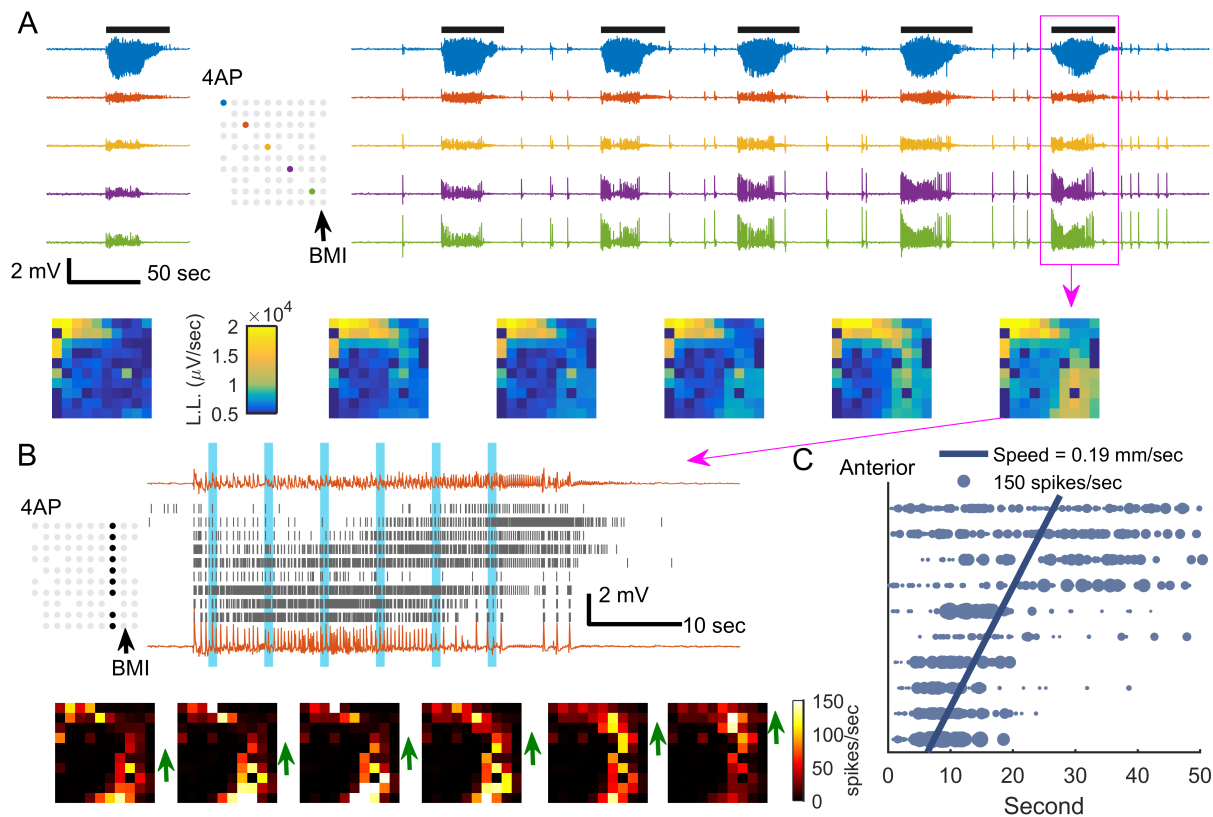
A. LFPs before (left) and after (right) BMI injection. Figure conventions are adopted from Figure 6A. Note that the ictal event at the BMI site is temporally linked with the 4-AP event but with quite a different electrographic morphology. Spatial distribution of ictal

activities of each ictal event is shown in the frames sequentially. L.L.: line-length. Notice the two physically separate ictal foci.

B. Multiunit activity during the ictal event marked with a magenta box in Panel A. Each row of the raster was recorded from the electrode whose physical position is marked in the inlet map (upper: anterior electrodes; lower: posterior electrodes). The upper and lower traces are the LFP recorded from the most anterior and the most posterior electrodes of the marked electrode column respectively. Spatiotemporal evolution of multiunit firing rates (1 sec Gaussian kernel for capturing expansion of ictal cores) are showed in the frames whose timing are indicated by the vertical blue bars at the raster plot. Green arrows indicate the propagation direction of multiunit activity.

C. Statistical analysis of anterior-posterior propagation of 4-AP ictal events after BMI injection. The horizontal coordinates indicate when a channel achieved its maximal firing rate (1 sec Gaussian kernel), and the vertical coordinates indicate its physical position anterior-posteriorly. Each datum was plotted with a size that is proportional to its maximum firing rate. Data from different animals are plotted with minor vertical offsets. Linear regression model: $t = \beta_0 + \beta_1 x$. N=846, 1 animal, 21 ictal events, 95% confidence interval: 0.17 to 0.21 mm/sec, F-test p << 0.001, Adjusted R^2 = 0.343.

Multifocal integration and epileptic network formation

We next investigated interactions between the two separate ictal foci (Figure 7). Non-negative matrix factorization, an unsupervised clustering algorithm, demonstrated that two

clusters of neuronal activity existed during the ictal events (1 animal, 21 ictal events, median residual squared error: 44%, interquartile range: 42.5 to 46.6%); each cluster had its spatial distribution near the 4-AP or BMI injection sites respectively (Figure 8A left subpanels). The 4-AP-cluster's neuronal dynamics (orange trace) showed complex interactions with the BMI-cluster (blue trace) – neuronal bursts at the BMI-cluster were able to trigger firing at the 4-AP cluster (blue box, right subpanels) and vice versa (red box). This 'ping-pong' effect had a short temporal delay, and the interaction of the two clusters occurred in both directions (Figure 8B). This may be described as an epileptic network with two physically separable nodes communicating along existing bidirectional excitatory pathways. The short signal delay between the two foci, 14 (red arrow) and 19 ms (blue arrow) respectively, is compatible with the delay time caused by an oligo-synaptic pathway.

Seizures with two dynamically distinct foci could also be observed by wide field calcium imaging. Using a similar experimental set-up, wide field calcium imaging demonstrated the existence of two dynamically distinct, yet linked foci. Although ictal events initiated at the same time, calcium dynamics only correlated with the immediately adjacent area corresponding with 2-3 mm focus (Figure 8C-D).

Figure 8 Ping-pong dynamics in distributed ictal zones
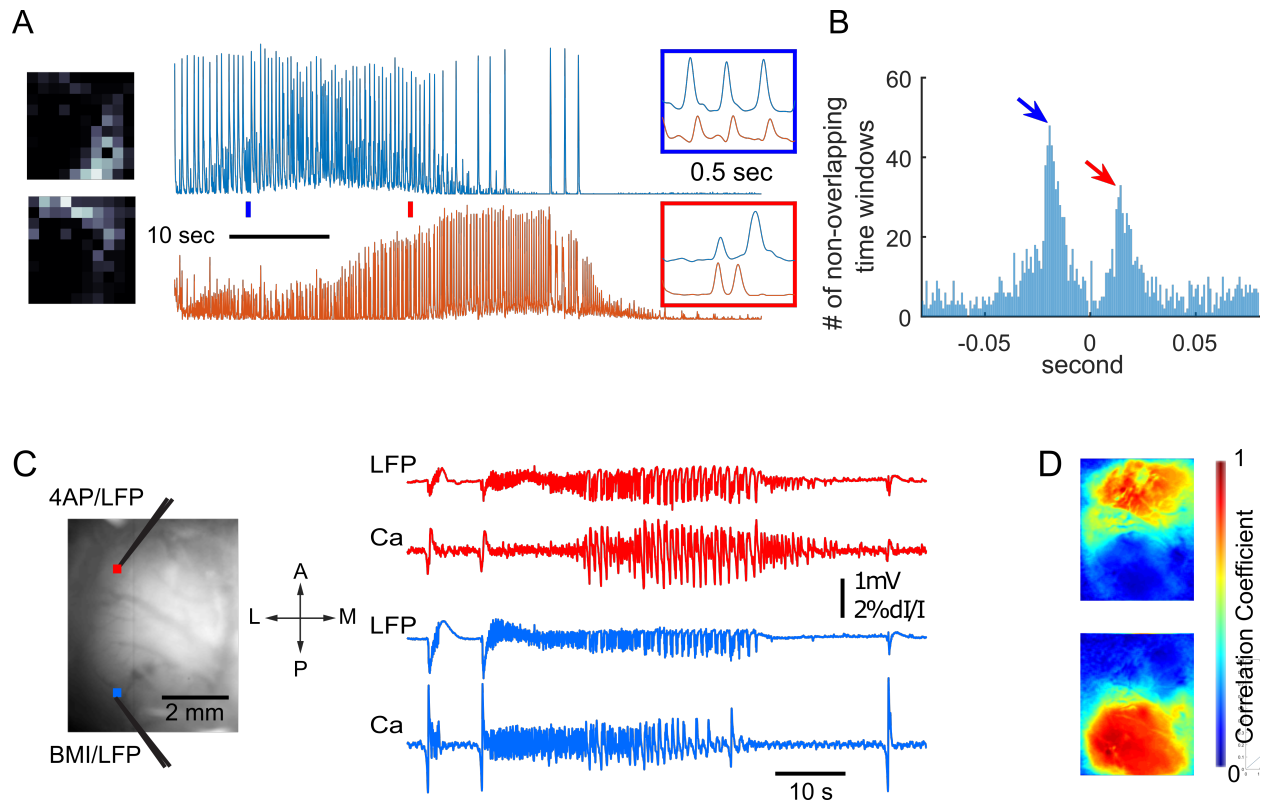
A. Factorization of neuronal dynamics. Multiunit spiking rates were estimated by 10 ms Gaussian kernel convolution every 1 ms. The resultant multivariate time series were factorized by non-negative matrix factorization (latent dimensionality = 2, residual Frobenius norm divided by the original matrix norm: 44%, interquartile range: 42.5 to 46.6%) Left panels: the distribution of the two non-negative factors (21 ictal events, 1037 seconds). Right traces: the temporal evolution of the weights of the two models during the sample event (the magenta box). The horizontal axis aligns with Panel C. The blue & red short segments are further zoomed in (inlet boxes) to illustrate the ping-pong dynamics. The blue box shows the blue factor temporally leads the red factor (BMI to 4AP corner); whereas the red box shows the opposite.

B. Cross-correlation study shows ping-pong dynamics. The multivariate time series calculated from Panel A were broken down into 2074 non-overlapping time windows (0.5 second each). The distribution of peak correlation times of miniepisodes are plotted. Notice the bimodal-like distribution of peak correlation times (red & blue arrows: -19 ms & 14 ms).

C. Wide field imaging of similar two focus experimental set-up. Left, the field of view, showing the location of 4-AP (red) and BMI (green) injection sites. Right, the LFP (top) and Ca signals (bottom, taken from ROI near electrode) recorded from 4-AP and BMI injection sites, respectively. Note that although the seizure onsets are temporally linked in that they start at the same time, the evolution of morphology of the ictal waveform is quite different as recorded both with the LFP and the calcium imaging.

D. The seed initiated correlation coefficient maps. Top: The seed trace is the Ca signal recorded from an ROI adjacent to the 4-AP injection site. Bottom: The seed trace is the Ca signal recorded from an ROI adjacent to the BMI injection site. Note, two distinct ictal foci are spatially separated indicating that each focus is distinct.

Cross-callosal projections are inadequate to recruit a second ictal focus following focal disinhibition

Finally, we investigated whether the same network dynamics could be served by cross-callosal synaptic projections, by creating an area of focal disinhibition in the contralateral hemisphere. A 4-AP ictal focus was created in left somatosensory cortex, and BMI was injected

in the contralateral (right) homotopic region. As expected, 4-AP ictal events emerged ipsilaterally while focal interictal spikes were observed at the contralateral site (Figure 9A). Ictal events did not propagate to the contralateral hemisphere, with no difference in contralateral LFP activity between ictal and interictal periods (Figure 9B) (p=0.805, 2 animals, 17 ictal events, 680 data points). Similarly, there was no consistent increase in average multiunit firing rates in the contralateral cortices during ictal periods in comparison to interictal periods (p = 0.98, Figure 9C-D). This finding was also supported by wide field calcium imaging (Figure 9E-F). Calcium fluorescence dynamics in the contralateral hemisphere showed little correlation to the 4-AP ictal focus (correlation coefficients: 0.068 ± 0.229, n = 7 rats). These results indicate that cross callosal projections are not capable of recruiting and synchronizing a second focus to create an epileptic network acutely (Figure 9F).

Figure 9. Injecting BMI at contralateral hemisphere cortices did not cause ictal propagation
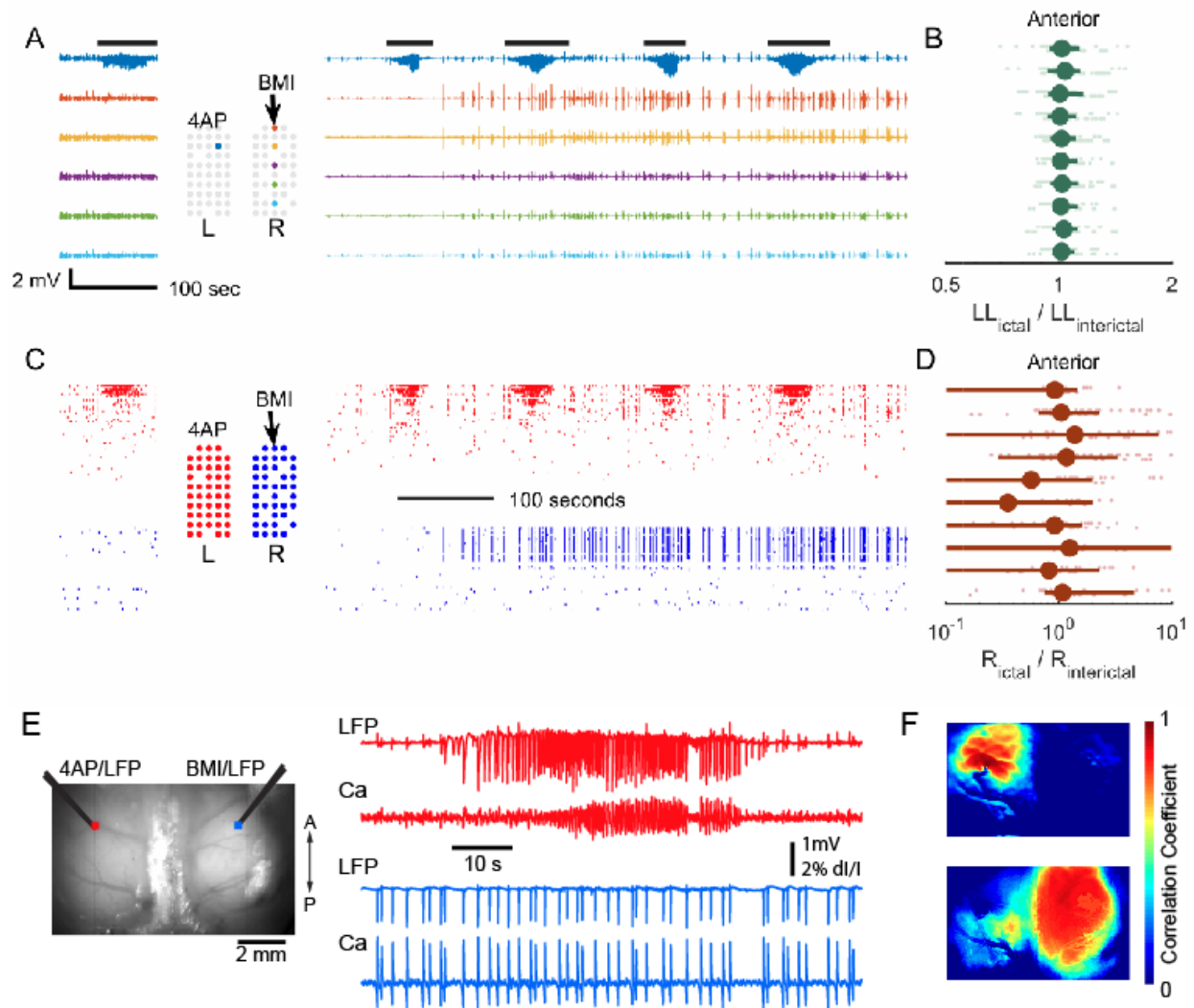
A. 4-AP is injected to create a seizure focus in the left hemisphere. LFP before (left) and after (right) BMI injection in the contralateral homotopic somatosensory cortex. After BMI injection, paroxysmal interictal spikes were seen in the LFP; however, a second ictal focus did not develop.

B. Comparison of line-length features during ictal versus interictal periods. For each channel during each ictal event, its line length was compared to the following interictal

period. A light green dot represents the analysis of one ictal event from one channel.

Data from different animals (N = 2) are plotted with minor vertical offsets for

visualization. Dark green dots represent medians and green bars indicate interquartile

ranges. Median $\frac{LL_{ictal}}{LL_{interictal}} = 1.02$, sign test under null hypothesis $LL_{ictal} = LL_{interictal}$,

p = 0.805.

C. Multiunit raster plot before (left) and after (right) BMI injection. Time is aligned with

Panel A.

D. Firing rate comparison between ictal versus interictal periods, analogous to Panel B. R

stands for average multiunit firing rate. Data were plotted similar to Panel B. Median

$\frac{R_{ictal}}{R_{interictal}} = 1.02$, sign test under null hypothesis $R_{ictal} = R_{interictal}$ 1, p = 0.98.

E. Wide field calcium imaging of 4-AP ictal focus in the left hemisphere and focal

disinhibition with BMI injected at the contralateral homotopic cortex. Left: the field of

view showing the injection sites. Right: The LFP and calcium fluorescence signal

recorded from 4AP (top) and BMI(bottom) injection sites. The ictal events do not

propagate to the contralateral side and the BMI injection results in focal interictal spikes

without creating a new interconnected ictal focus.

F. The seed initiated correlation coefficient maps. Top: the seed trace used was taken from

an ROI adjacent to the 4-AP injection site. Bottom: the seed trace used was taken from

an ROI adjacent to the BMI injection site. The ictal even remains focal and does not

involve the other hemisphere. The disinhibited interictal spiking zone is widespread and

completely independent from the seizure focus.

Discussion

We investigated local and distant neural responses to focal neocortical ictal events in an acute pharmacologically induced seizure model. Recording data from both two-dimensional microelectrode arrays and calcium imaging confirmed the existence of strong, widespread synaptic projections. Ictal events triggered by focal application of 4-AP remained confined to a small cortical territory, but displayed various propagation patterns when BMI was added focally or globally from the 4-AP site. The observed spread patterns and temporal delays of ictal discharges were consistent with activation of large-scale excitatory synaptic pathways in the ipsilateral hemisphere, through which the success of seizure transmission depends on impairment of the GABA-A mediated inhibitory restraint. These data indicate that large-scale seizure spread and epileptic network formation may coexist with the classical model of contiguous cortical Jacksonian propagation, both involving the breakdown of inhibitory restraint. Further, the coupling of the two foci occurred acutely in normal brain, implying that pathological structural alterations are not required for this to occur.

Previously, we characterized brain areas where principle neurons demonstrate intense, synchronized burst firing (i.e. clonic firing) temporally locked to LFP discharges as the "ictal core" (Schevon et al., 2012). This region is sharply demarcated (Smith et al., 2016). Regions outside the ictal core that are not directly participating in the seizure, but still receive significant, potentially ictogenic excitatory projections from it, are termed the "ictal penumbra". Synaptic activity in the penumbra is time-locked to that in the ictal core, consisting of a mixture of excitatory and inhibitory field potentials, with pyramidal cell firing restrained by the inhibitory veto. This results in relatively sparse, heterogeneous firing that is generally not phase-locked to

the low-frequency LFP (Schevon et al., 2012; Truccolo et al., 2011; Weiss et al., 2013). Thus, in normally functioning penumbra, the effects of strong widespread excitation are masked by local inhibitory responses. Thus, the ictal penumbra may be considered similarly to its counterpart in the stroke literature, as a brain region influenced by the ongoing seizure and at risk of seizure invasion. In our acute rodent neocortical model, this brain region contains more than the immediate surround, widely including the ipsilateral hemisphere but not the contralateral hemisphere, as evidenced by the fact that seizures can propagate to distant sites once the inhibition veto is lifted.

The core-penumbra coupling mechanism is suggested in the morphology of LFP deflections associated with synchronized neuronal bursts during ictal events. The observed polarity flip (proximal-negative versus distal-positive) and temporal delay (~10 ms) suggests that nearby regions are dominated by monosynaptic local recurrent excitatory projections arising from pyramidal neurons within the ictal zone, while distant territories are dominated by di-synaptic feedforward inhibition, involving projections to inhibitory interneurons (Marshall et al., 2016). These observations are not consistent with a passive volume-conducted process, as we would then expect preserved polarity and minimal temporal delays.

PV(+) interneurons are physiologically well-positioned to exert the inhibitory veto (Cammarota et al., 2013; Pouille et al., 2013; Sessolo et al., 2015). Their small size, high input resistance, and low rheobase make them sensitive to synchronized excitation input (Kepecs and Fishell, 2014; Markram et al., 2004). Their perisomatic projection makes them good candidates for exerting a sufficiently strong inhibitory effect to prevent ictal invasion (Pfeffer et al., 2013). Two-photon calcium imaging confirmed that PV(+) interneurons responded rapidly to distal

ictal events (somatosensory to visual cortices). The strong inhibitory post-synaptic response is a likely source of the polarity flip seen in our spike-triggered averaging study.

We selected the 4-AP model (Ma et al., 2013; Ma et al., 2009; Szente and Baranyi, 1987; Szente and Pongracz, 1979; Zhao et al., 2009; Zhao et al., 2015; Zhao et al., 2011) due to its ability to trigger a well-defined, spatially limited (~2-3 mm diameter) neocortical ictal event, electrographically mimicking spontaneous human neocortical seizures with a low-voltage fast activity onset pattern. We demonstrated that the region of actively spiking remains focal throughout the evolution of the seizure, as long as the surrounding inhibitory mechanisms are intact. This focality permitted us to place the BMI site at varying fixed distances in order to assess interactions between the core and surrounding areas. In a chronic model, the site of seizure origination is less well defined, and cortical propagation is likely to occur spontaneously without a pharmacologically-induced breakdown of inhibition. While our use of an acute model may limit applicability to chronic human epilepsy, it was necessary in order to create the simple structure needed to test our hypothesis. The use of an acute model also allowed us to determine that complex epileptic network interactions do not require established pathological connectivity.

We found the two topologically distinct seizure propagation patterns can arise from a similar process of inhibition breakdown; however, the physiological mechanisms leading to it may differ subtly in vivo. At the juxta-ictal core region, both synaptic as well as extracellular mechanisms, i.e. potassium diffusion and field effects, may contribute to the breakdown of inhibition (Bikson et al., 2003; Frohlich et al., 2008; Mylvaganam et al., 2014; Park and Durand, 2006; Pumain et al., 1985; Zhang et al., 2014), resulting in classical Jacksonian march-like

propagation (Schevon et al., 2012). In contrast, inhibition compromise at a distal site may be attributed to synaptic mechanisms, such as intracellular chloride accumulation (Barmashenko et al., 2011; Buchin et al., 2016; Huberfeld et al., 2007; Lillis et al., 2012), synchronization (Jiruska et al., 2013; Lehnertz et al., 2009), or regional variation of inhibition robustness.

Two dynamically distinct ictal foci emerged in the experiments involving separate 4AP and BMI injection sites. Most commonly, seizure expansion toward the BMI site was seen, with nearly simultaneous onsets at both locations that would be hard to tease apart by examining LFPs alone. Ping-ponging indicated that once begun, a two-way excitatory dynamic was created. In some instances, seizure activity was restricted to regions close to the two foci, with the seizure appearing to "jump" across the gap. This provides proof of principle that seizures can generate secondary foci that appear to operate as a unified network. Analysis of temporal delays during ictal events can be a rich source of information, but the observed 'ping-ponging' between the foci indicates complex, bilaterally directed coupling dynamics could complicate the picture.

A key observation regarding the epileptic activity observed at the BMI site is that the oscillatory pattern was similar to 4-AP triggered seizures, rather than the high amplitude bursts of the BMI model. The high amplitude, repetitive epileptiform discharges triggered by BMI were occasionally seen independently, as shown in the cross-hemisphere experiment in Figure 9. The appearance of a 4AP-type seizure at the BMI injection site is a strong demonstration that the source of the seizure at this site was the distant 4-AP focus, rather than being solely attributable to BMI.

In conclusion, our study shows that focal ictal events project strong excitation widely over ipsilateral hemisphere in an acute rodent seizure model. Compromised local inhibitory response, depending on its distance from the ictal core, can result in various seizure propagation patterns and epileptic network formation. Further studies are required to discriminate various distance-dependent seizure defense mechanisms.

Materials and Methods

All experimental procedures were approved by either the Weill Cornell Medical College or Columbia University Animal Care and Use Committee following the National Institutes of Health guidelines. Three experimental modalities are used in this study – multielectrode array recording, wide-field calcium imaging, and two-photon calcium imaging. The corresponding experimental procedures and analyses are listed below.

Multielectrode array recording

Animal preparation. Adult male Sprague–Dawley rats (200–350 g) were anesthetized with isoflurane in 70% N_2:30% O_2, 4% induction, and 1.5–2% maintenance. Body temperature was maintained at 37 °C with a regulated heating blanket (Harvard Apparatus, Holliston, MA). The heart rate, pO_2, and the end tidal carbon dioxide ($EtCO_2$) were carefully monitored with a small animal capnography (Surgivet, Waukesha, WI) and were sustained throughout the experiment (heart rate: 250–300 pulse/minute, pO2 > 90%, $EtCO_2 \sim$ 25–28 mmHg). The exposed brain was covered with cotton balls socked with artificial cerebrospinal fluid (ACSF) to preserve cortical moisture.

Array configuration. Two types of multielectrode arrays were used in this study. The first type, used for unilateral (left) hemisphere recording, was configured into a 10 by 10 grid with 400 μm interelectrode distance (Blackrock Microsystems Inc, Salt Lake City, UT). The second type, used for bilateral hemisphere recording, was configured into two separate 10 by 5 grids with 400 μm

interelectrode distance. Both types of arrays were implanted into the cortex with a 0.5 mm

pneumatic implanter (Blackrock Microsystems Inc, Salt Lake City, UT)(Rousche and Normann,

1992). The grids' anterior edges met the animal's somatosensory cortices (Figure 2A). In the

bilateral array experiment, the long side (10 electrodes) was aligned anterior-posteriorly, and

each grid was used for each hemisphere. Reference electrodes were placed subdurally, distal

to recording sites, and dynamically selected to minimize reference artifacts.

Array Signal recording. Raw electrical signal was digitally sampled at 30 kHz with 16-bit

precision (range ±8 mV, resolution 0.25 μV, 0.3 to 7500 Hz band pass). Raw data were

subsequently separated into two frequency bands: multiunit activity (MUA, 300 to 3000 Hz,

512th order zero-phase shift, window-based FIR filter). LFP was derived by downsampling the

raw signal to 1 k Hz after anti-alias filtering (500 Hz low-pass, 90th order, zero-phase shift,

window-based FIR filter). Channels with background noise amplitude (estimated by scaled

median absolute deviation) more than 8 µV in MUA band or excessive paroxysmal artifacts

were discarded (Quiroga et al., 2004).

Multiunit spike detection & firing rate estimation. Multiunit spikes were detected from the

MUA band by a threshold crossing method(Quiroga et al., 2004). Each channel's detection

threshold was set to be -5 s.d. of the channel's background noise (estimated from a 2-minute

baseline recording). Detection refractory period was set to be 1 ms, to minimize detection of

multiple peaks due to noise. Channels that failed to detect more than 1 multiunit spike per

minute were also excluded.   For each channel, instantaneous multiunit firing rates were

estimated by convolving its spike train with Gaussian kernels, sampled every 1 ms (Bokil et al.,

2010; Shimazaki and Shinomoto, 2010; Smith et al., 2016). Two types of Gaussian kernels were used in this study: a 10-ms s.d. Gaussian kernel for capturing rapid change of multiunit firing rates and a 1-second s.d. kernel for slow change of average firing rates.

Seizure model. 4-Aminopyridine (4-AP, Sigma-Aldrich, 15 mM, 500 nL), a potassium channel blocker, was injected at the anterior edge of the array in the left somatosensory cortex, targeting 300–500 µm below the cortical surface through a glass microelectrode using a Nanoject II injector (Drummond Scientific, Broomall, PA) (Avoli et al., 2016; de Curtis and Avoli, 2016; Pongracz and Szente, 1979; Rutecki et al., 1987) after a 2-minute baseline recording. The 4-AP dose was increased to 1000 nL if electrographic seizures were not observed in the next 20 minutes of recording. 30 to 60 minutes after the first electrographic seizure, bicuculline methiodide (BMI, Sigma-Aldrich, 5 mM), a GABA-A receptor antagonist, was introduced either by bath application (left hemisphere) or focal injection (500nL, 300–500 µm depth at left visual cortex or right somatosensory cortex). Neural dynamics were recorded for another 30 to 60 minutes following BMI injection.

Ictal activity detection and quantification. The line-length feature of LFP was used to quantify ictal activity and facilitate systematic and objective ictal event detection (Esteller et al., 2001; Guo et al., 2010). For each channel, line-length was calculated for 1-second moving windows (step size: 1 ms). Periods that had more than 3 channels demonstrating greater than 3 times more line-length than the baseline and lasted for more than 5 seconds were considered as ictal event candidates, which were further visually reviewed to exclude artifacts. The onset and offset of ictal events were adjusted manually to encompass all epileptiform discharges.

Furthermore, two ictal events were required to be at least 20 seconds apart temporally to be considered two isolated episodes (Ma et al., 2009; Zhao et al., 2009; Zhao et al., 2011). The periods between two consecutive ictal events are defined as interictal periods. For each ictal event, the ictal center is defined as physical location of the electrode where we detected the highest line-length.

Multiunit spike-LFP coupling. We used spike-triggered averaging to investigate the association between multiunit firing and LFP dynamics of the entire region sampled by microelectrodes (Eissa et al., 2016; Schwartz et al., 2006). Multiunit spikes which were detected within 1 mm from the ictal center were combined to create the spike train used for averaging.

Cross-correlation of multiunit spike trains. Cross-correlation between binned spike-trains (1 ms resolution) was used to determine the temporal relationships between any two spike trains. The timing of peak cross-correlation, $\Delta t_{a,b} = \mathrm{argmax}_\tau\, C_{a,b}(\tau)$, was defined as the temporal delay between two channels, a and b.

Cluster analysis of multiunit spike trains. Non-negative matrix factorization was applied to study the clustering phenomenon of ictal dynamics (Hutchins et al., 2008; Lee and Seung, 1999). During each ictal event, each channel's instantaneous multiunit firing rate was determined by convolution with a 10-ms s.d. Gaussian kernel. The resultant time series were aligned in rows and assembled into a data matrix, A, where $A_{i,j}$ is the instantaneous firing rate of channel i at time j. The matrix, A, consisting of all non-negative entries, was further factorized into two non-negative matrices, $A \approx WH$ with latent dimensionality $k = 2$. The interaction between the latent dynamics were further investigated using cross-correlation.

Wide-field Calcium Imaging

Calcium dye loading and fluorescence measurement. The calcium indicator Oregon Green 488 BAPTA-1 AM (OGB-1, Life Technologies, Grand Island, New York) was employed for recording of neural activity. Convection enhanced delivery (CED) was employed to bulk load the entire neocortex with OGB-1(Ma et al., 2014). In brief, 50 μg of OGB-1 was diluted in 5 μL of DMSO-F127 then in 50 μL of ACSF. 8 μL of OGB-1 solution was injected in the neocortex, via a glass electrode (50-100 μm opening) placed ~1 mm below the brain surface, at the speed of 100 nL/min, using a micro-pump (WPI, Sarasota, Florida). A CCD camera (Dalsa camera in Imager 3001, Optical Imaging, Rehovot, Israel) using a tandem lens (50 × 50 mm) arrangement was focused 300–400 μm below the cortical surface. A 470$\pm$10 nm LED was employed as the illumination source for calcium-sensitive dye and illumination was directed using fiber-optic light guides. A 510 nm long-pass filter was placed before the camera to prevent calcium illumination contamination, while permitting calcium dye signal.

Calcium imaging analysis. Data were analyzed by customized MATLAB functions. Calcium images were convolved with a spatial Gaussian kernel (σ = 3 pixels) to increase signal-to-noise ratio. The signal changes were calculated as dF/F, where F was the baseline illumination when no epileptiform discharges were noticed and dF was the signal change during epileptiform activity as identified by the LFP. A 1 Hz high-pass filter was applied to the calcium imaging data to remove the calcium signal from glial cells.

A seed trace initiated correlation method(White et al., 2011) was employed to calculate the spatial spread of neuronal activity. Briefly, a seed trace was selected from a small region of interest (ROI) from the 4-AP and BMI injection sites. The correlation coefficients between the seed trace and trace from every individual pixel in the surrounding image were calculated. A heat map was generated using the correlation coefficient (CC) at each pixel.

Two-photon Calcium Imaging

Animal preparation, seizure model, and ictal event detection. PV-Cre mice (RRID:IMSR_JAX:017320) were crossed with LSL-GCaMP6F(Chen et al., 2013) mice (RRID:IMSR_JAX:024105), resulting in GCaMP6F expression specifically in parvalbumin (PV) positive interneurons. Animals were anesthetized and their physiological conditions were maintained similarly to protocols described in previous sections. Two craniotomies over the left hemisphere were created – one (visual cortex) for 4-AP (15 mM, 500 nL) injection and the other (somatosensory cortex, 4 mm away from 4-AP injection site) for imaging.

Image collection. Calcium imaging of GCaMP6F positive interneurons was performed using a two-photon microscope (Bruker; Billerica, MA) and a Ti:Sapphire laser (Chameleon Ultra II; Coherent) using a 25x objective (water immersion, N.A. 1.05, Olympus). GCaMP6F was excited with a laser wavelength of 940 nm, fluorescence emission was collected through a 535nm (green) filter (Chroma, Bellows Falls, VT). Resonant galvanometer scanning and image

acquisition (frame rate 30,206 fps, 512 x 512 pixels, 150-200 μm below the pial surface) were controlled by Prairie View Imaging software.

Image analysis. Regions of interest (ROIs) were registered manually to target GCaMP6F-expressing PV(+) interneurons using ImageJ (National Institute of Mental Health, Bethesda, MD.). To minimize cell signal contamination by surround neuropil fluorescence changes, we applied ROI shrinkage (Radial subtraction of 1 pixel from somatic ROI)(Hofer et al., 2011). Individual cell fluorescence was calculated as the average across all pixels within the ROI. Then, we calculated relative changes in fluorescence (F) as $\frac{\Delta F(t)}{F_0} = \frac{(F(t)-F_0)}{F_0}$, where F_0 represents the mean of the lowest 25% of values within a 500-frame window centered around each value F(t). Finally, to minimize tissue pulsation artifacts in the extracted traces, individual traces were filtered with a 2-second LOWESS smoothing envelope.

Ictal events – PV interneuron activity coupling. LFP, recorded from a glass micropipette (2-5 MΩ, AgCl wire in isotonic PBS solution) 100 μm beneath the pial surface near the 4-AP injection site, were used for ictal event detection. A reference electrode was positioned over the contralateral frontal cortex. LFP signals were amplified by a Multiclamp 700B amplifier (Axon Instruments, Sunnyvale, CA), low-pass filtered (300 Hz, Multiclamp 700B commander software, Axon Instruments), digitized at 1000 Hz (Bruker) and recorded using Prairie View Voltage Recording Software along with calcium imaging. Ictal events were inspected visually. Specific ictal onset time was determined by searching the turning point of initial negative DC-shift:

$t_{onset} = \mathrm{argmin}_\tau \ddot{V}(\tau).$

To calculate time lags between individual ictal onsets (measured by LFP within the seizure initiation site) and the respective time of local PV population recruitment at the FOV (distance to initiation site ca. 4 mm), we derived an average calcium transient of all imaged PVs in the FOV. Then, we defined timing of maximum curvature (most negative 2nd derivative) of the population calcium transient during each peri-ictal onset window (centered around the time point of the electrographic seizure onset) as the time point of PV population recruitment. Eventually, the lag was calculated as $\Delta t_{seizure} = t_{calcium} - t_{LFP}$.

Competing interests:

All authors report that there are no competing interests.

References:

Avoli, M., and de Curtis, M. (2011). GABAergic synchronization in the limbic system and its role in the generation of epileptiform activity. Progress in neurobiology *95*, 104-132.

Avoli, M., de Curtis, M., Gnatkovsky, V., Gotman, J., Kohling, R., Levesque, M., Manseau, F., Shiri, Z., and Williams, S. (2016). Specific imbalance of excitatory/inhibitory signaling establishes seizure onset pattern in temporal lobe epilepsy. Journal of neurophysiology *115*, 3229-3237.

Bahar, S., Suh, M., Zhao, M., and Schwartz, T.H. (2006). Intrinsic optical signal imaging of neocortical seizures: the 'epileptic dip'. Neuroreport *17*, 499-503.

Barmashenko, G., Hefft, S., Aertsen, A., Kirschstein, T., and Kohling, R. (2011). Positive shifts of the GABAA receptor reversal potential due to altered chloride homeostasis is widespread after status epilepticus. Epilepsia *52*, 1570-1578.

Bikson, M., Fox, J.E., and Jefferys, J.G. (2003). Neuronal aggregate formation underlies spatiotemporal dynamics of nonsynaptic seizure initiation. Journal of neurophysiology *89*, 2330-2333.

Bokil, H., Andrews, P., Kulkarni, J.E., Mehta, S., and Mitra, P.P. (2010). Chronux: a platform for analyzing neural signals. Journal of neuroscience methods *192*, 146-151.

Buchin, A., Chizhov, A., Huberfeld, G., Miles, R., and Gutkin, B.S. (2016). Reduced Efficacy of the KCC2 Cotransporter Promotes Epileptic Oscillations in a Subiculum Network Model. The Journal of neuroscience : the official journal of the Society for Neuroscience *36*, 11619-11633.

Cammarota, M., Losi, G., Chiavegato, A., Zonta, M., and Carmignoto, G. (2013). Fast spiking interneuron control of seizure propagation in a cortical slice model of focal epilepsy. The Journal of physiology *591*, 807-822.

Chagnac-Amitai, Y., and Connors, B.W. (1989). Horizontal spread of synchronized activity in neocortex and its control by GABA-mediated inhibition. Journal of neurophysiology *61*, 747-758.

Chen, T.W., Wardill, T.J., Sun, Y., Pulver, S.R., Renninger, S.L., Baohan, A., Schreiter, E.R., Kerr, R.A., Orger, M.B., Jayaraman, V.*, et al.* (2013). Ultrasensitive fluorescent proteins for imaging neuronal activity. Nature *499*, 295-300.

de Curtis, M., and Avoli, M. (2016). GABAergic networks jump-start focal seizures. Epilepsia.

Eissa, T.L., Tryba, A.K., Marcuccilli, C.J., Ben-Mabrouk, F., Smith, E.H., Lew, S.M., Goodman, R.R., McKhann, G.M., Jr., Frim, D.M., Pesce, L.L.*, et al.* (2016). Multiscale Aspects of Generation of High-Gamma Activity during Seizures in Human Neocortex. eNeuro *3*.

Esteller, R., Echauz, J., Tcheng, T., Litt, B., and Pless, B. (2001). Line length: An efficient feature for seizure onset detection. P Ann Int Ieee Embs *23*, 1707-1710.

Extercatte, J., de Haan, G.J., and Gaitatzis, A. (2015). Teaching Video NeuroImages: Frontal opercular seizures with jacksonian march. Neurology *84*, e83-84.

Frohlich, F., Bazhenov, M., Iragui-Madoz, V., and Sejnowski, T.J. (2008). Potassium dynamics in the epileptic cortex: new insights on an old topic. The Neuroscientist : a review journal bringing neurobiology, neurology and psychiatry *14*, 422-433.

Geneslaw, A.S., Zhao, M., Ma, H., and Schwartz, T.H. (2011). Tissue hypoxia correlates with intensity of interictal spikes. J Cereb Blood Flow Metab *31*, 1394-1402.

Guo, L., Rivero, D., Dorado, J., Rabunal, J.R., and Pazos, A. (2010). Automatic epileptic seizure detection in EEGs based on line length feature and artificial neural networks. Journal of neuroscience methods *191*, 101-109.

Hofer, S.B., Ko, H., Pichler, B., Vogelstein, J., Ros, H., Zeng, H., Lein, E., Lesica, N.A., and Mrsic-Flogel, T.D. (2011). Differential connectivity and response dynamics of excitatory and inhibitory neurons in visual cortex. Nature neuroscience *14*, 1045-1052.

Huberfeld, G., Wittner, L., Clemenceau, S., Baulac, M., Kaila, K., Miles, R., and Rivera, C. (2007). Perturbed chloride homeostasis and GABAergic signaling in human temporal lobe epilepsy. The Journal of neuroscience : the official journal of the Society for Neuroscience *27*, 9866-9873.

Hutchins, L.N., Murphy, S.M., Singh, P., and Graber, J.H. (2008). Position-dependent motif characterization using non-negative matrix factorization. Bioinformatics *24*, 2684-2690.

Jiruska, P., de Curtis, M., Jefferys, J.G., Schevon, C.A., Schiff, S.J., and Schindler, K. (2013). Synchronization and desynchronization in epilepsy: controversies and hypotheses. The Journal of physiology *591*, 787-797.

Kepecs, A., and Fishell, G. (2014). Interneuron cell types are fit to function. Nature *505*, 318-326.

Khambhati, A.N., Davis, K.A., Lucas, T.H., Litt, B., and Bassett, D.S. (2016). Virtual Cortical Resection Reveals Push-Pull Network Control Preceding Seizure Evolution. Neuron *91*, 1170-1182.

Kramer, M.A., Eden, U.T., Kolaczyk, E.D., Zepeda, R., Eskandar, E.N., and Cash, S.S. (2010). Coalescence and fragmentation of cortical networks during focal seizures. The Journal of neuroscience : the official journal of the Society for Neuroscience *30*, 10076-10085.

Lee, D.D., and Seung, H.S. (1999). Learning the parts of objects by non-negative matrix factorization. Nature *401*, 788-791.

Lehnertz, K., Bialonski, S., Horstmann, M.T., Krug, D., Rothkegel, A., Staniek, M., and Wagner, T. (2009). Synchronization phenomena in human epileptic brain networks. Journal of neuroscience methods *183*, 42-48.

Lillis, K.P., Kramer, M.A., Mertz, J., Staley, K.J., and White, J.A. (2012). Pyramidal cells accumulate chloride at seizure onset. Neurobiology of disease *47*, 358-366.

Lopantsev, V., and Avoli, M. (1998). Participation of GABAA-mediated inhibition in ictallike discharges in the rat entorhinal cortex. Journal of neurophysiology *79*, 352-360.

Luo, C., An, D., Yao, D., and Gotman, J. (2014). Patient-specific connectivity pattern of epileptic network in frontal lobe epilepsy. Neuroimage Clin *4*, 668-675.

Ma, H., Zhao, M., Harris, S., and Schwartz, T.H. (2014). Simultaneous multi-wavelength optical imaging of neuronal and hemodynamic activity. In Neurovascular Coupling Methods, pp. 237-249.

Ma, H., Zhao, M., and Schwartz, T.H. (2013). Dynamic neurovascular coupling and uncoupling during ictal onset, propagation, and termination revealed by simultaneous in vivo optical imaging of neural activity and local blood volume. Cerebral cortex *23*, 885-899.

Ma, H., Zhao, M., Suh, M., and Schwartz, T.H. (2009). Hemodynamic surrogates for excitatory membrane potential change during interictal epileptiform events in rat neocortex. Journal of neurophysiology *101*, 2550-2562.

Ma, H.T., Wu, C.H., and Wu, J.Y. (2004). Initiation of spontaneous epileptiform events in the rat neocortex in vivo. Journal of neurophysiology *91*, 934-945.

Markram, H., Toledo-Rodriguez, M., Wang, Y., Gupta, A., Silberberg, G., and Wu, C. (2004). Interneurons of the neocortical inhibitory system. Nat Rev Neurosci *5*, 793-807.

Marshall, J.D., Li, J.Z., Zhang, Y., Gong, Y., St-Pierre, F., Lin, M.Z., and Schnitzer, M.J. (2016). Cell-Type-Specific Optical Recording of Membrane Voltage Dynamics in Freely Moving Mice. Cell *167*, 1650-1662 e1615.

Merricks, E.M., Smith, E.H., McKhann, G.M., Goodman, R.R., Bateman, L.M., Emerson, R.G., Schevon, C.A., and Trevelyan, A.J. (2015). Single unit action potentials in humans and the effect of seizure activity. Brain : a journal of neurology *138*, 2891-2906.

Mylvaganam, S., Ramani, M., Krawczyk, M., and Carlen, P.L. (2014). Roles of gap junctions, connexins, and pannexins in epilepsy. Front Physiol *5*, 172.

Park, E.H., and Durand, D.M. (2006). Role of potassium lateral diffusion in non-synaptic epilepsy: a computational study. Journal of theoretical biology *238*, 666-682.

Pfeffer, C.K., Xue, M., He, M., Huang, Z.J., and Scanziani, M. (2013). Inhibition of inhibition in visual cortex: the logic of connections between molecularly distinct interneurons. Nature neuroscience *16*, 1068-1076.

Pinto, D.J., Patrick, S.L., Huang, W.C., and Connors, B.W. (2005). Initiation, propagation, and termination of epileptiform activity in rodent neocortex in vitro involve distinct mechanisms. The Journal of neuroscience : the official journal of the Society for Neuroscience *25*, 8131-8140.

Pongracz, F., and Szente, M. (1979). Simulation of the ionic mechanisms of molluscan neurons under pentylenetetrazol-induced effects. Acta physiologica Academiae Scientiarum Hungaricae *53*, 327-336.

Pouille, F., Watkinson, O., Scanziani, M., and Trevelyan, A.J. (2013). The contribution of synaptic location to inhibitory gain control in pyramidal cells. Physiol Rep *1*, e00067.

Pumain, R., Menini, C., Heinemann, U., Louvel, J., and Silva-Barrat, C. (1985). Chemical synaptic transmission is not necessary for epileptic seizures to persist in the baboon Papio papio. Experimental neurology *89*, 250-258.

Quiroga, R.Q., Nadasdy, Z., and Ben-Shaul, Y. (2004). Unsupervised spike detection and sorting with wavelets and superparamagnetic clustering. Neural computation *16*, 1661-1687.

Rousche, P.J., and Normann, R.A. (1992). A method for pneumatically inserting an array of penetrating electrodes into cortical tissue. Ann Biomed Eng *20*, 413-422.

Rutecki, P.A., Lebeda, F.J., and Johnston, D. (1987). 4-Aminopyridine produces epileptiform activity in hippocampus and enhances synaptic excitation and inhibition. Journal of neurophysiology *57*, 1911-1924.

Schevon, C.A., Weiss, S.A., McKhann, G., Jr., Goodman, R.R., Yuste, R., Emerson, R.G., and Trevelyan, A.J. (2012). Evidence of an inhibitory restraint of seizure activity in humans. Nature communications *3*, 1060.

Schwartz, O., Pillow, J.W., Rust, N.C., and Simoncelli, E.P. (2006). Spike-triggered neural characterization. J Vis *6*, 484-507.

Sessolo, M., Marcon, I., Bovetti, S., Losi, G., Cammarota, M., Ratto, G.M., Fellin, T., and Carmignoto, G. (2015). Parvalbumin-Positive Inhibitory Interneurons Oppose Propagation But Favor Generation of Focal Epileptiform Activity. The Journal of neuroscience : the official journal of the Society for Neuroscience *35*, 9544-9557.

Shimazaki, H., and Shinomoto, S. (2010). Kernel bandwidth optimization in spike rate estimation. Journal of computational neuroscience *29*, 171-182.

Smith, E.H., Liou, J.Y., Davis, T.S., Merricks, E.M., Kellis, S.S., Weiss, S.A., Greger, B., House, P.A., McKhann Ii, G.M., Goodman, R.R.*, et al.* (2016). The ictal wavefront is the spatiotemporal source of discharges during spontaneous human seizures. Nature communications *7*, 11098.

Smith, E.H., and Schevon, C.A. (2016). Toward a Mechanistic Understanding of Epileptic Networks. Curr Neurol Neurosci Rep *16*, 97.

Szente, M., and Baranyi, A. (1987). Mechanism of aminopyridine-induced ictal seizure activity in the cat neocortex. Brain research *413*, 368-373.

Szente, M., and Pongracz, F. (1979). Aminopyridine-induced seizure activity. Electroencephalogr Clin Neurophysiol *46*, 605-608.

Trevelyan, A.J., Baldeweg, T., van Drongelen, W., Yuste, R., and Whittington, M. (2007a). The source of afterdischarge activity in neocortical tonic-clonic epilepsy. The Journal of neuroscience : the official journal of the Society for Neuroscience *27*, 13513-13519.

Trevelyan, A.J., Sussillo, D., Watson, B.O., and Yuste, R. (2006). Modular propagation of epileptiform activity: evidence for an inhibitory veto in neocortex. The Journal of neuroscience : the official journal of the Society for Neuroscience *26*, 12447-12455.

Trevelyan, A.J., Sussillo, D., and Yuste, R. (2007b). Feedforward inhibition contributes to the control of epileptiform propagation speed. The Journal of neuroscience : the official journal of the Society for Neuroscience *27*, 3383-3387.

Truccolo, W., Donoghue, J.A., Hochberg, L.R., Eskandar, E.N., Madsen, J.R., Anderson, W.S., Brown, E.N., Halgren, E., and Cash, S.S. (2011). Single-neuron dynamics in human focal epilepsy. Nature neuroscience *14*, 635-641.

Uva, L., Librizzi, L., Wendling, F., and de Curtis, M. (2005). Propagation dynamics of epileptiform activity acutely induced by bicuculline in the hippocampal-parahippocampal region of the isolated Guinea pig brain. Epilepsia *46*, 1914-1925.

Weiss, S.A., Banks, G.P., McKhann, G.M., Jr., Goodman, R.R., Emerson, R.G., Trevelyan, A.J., and Schevon, C.A. (2013). Ictal high frequency oscillations distinguish two types of seizure territories in humans. Brain : a journal of neurology *136*, 3796-3808.

White, B.R., Bauer, A.Q., Snyder, A.Z., Schlaggar, B.L., Lee, J.M., and Culver, J.P. (2011). Imaging of functional connectivity in the mouse brain. PloS one *6*, e16322.

Zhang, M., Ladas, T.P., Qiu, C., Shivacharan, R.S., Gonzalez-Reyes, L.E., and Durand, D.M. (2014). Propagation of epileptiform activity can be independent of synaptic transmission, gap junctions, or diffusion and is consistent with electrical field transmission. The Journal of neuroscience : the official journal of the Society for Neuroscience *34*, 1409-1419.

Zhao, M., Ma, H., Suh, M., and Schwartz, T.H. (2009). Spatiotemporal dynamics of perfusion and oximetry during ictal discharges in the rat neocortex. The Journal of neuroscience : the official journal of the Society for Neuroscience *29*, 2814-2823.

Zhao, M., McGarry, L.M., Ma, H., Harris, S., Berwick, J., Yuste, R., and Schwartz, T.H. (2015). Optical triggered seizures using a caged 4-Aminopyridine. Frontiers in neuroscience *9*, 25.

Zhao, M., Nguyen, J., Ma, H., Nishimura, N., Schaffer, C.B., and Schwartz, T.H. (2011). Preictal and ictal neurovascular and metabolic coupling surrounding a seizure focus. The Journal of neuroscience : the official journal of the Society for Neuroscience *31*, 13292-13300.